



## Acoustofluidic micromixer on lab-on-a-foil devices

Yang Lin, Can Gao, Yuan Gao, Mengren Wu, Alireza Ahmadian Yazdi, Jie Xu\*

Department of Mechanical and Industrial Engineering, University of Illinois at Chicago, Chicago, IL 60607, USA



### ARTICLE INFO

#### Keywords:

Lab-on-a-foil  
Acoustic  
Film  
Two-photon polymerization  
Micromixing

### ABSTRACT

In this paper, off-the-shelf materials such as polyethylene terephthalate films and double-sided tapes are applied to create lab-on-a-foil microfluidic devices via a cutting plotter. Microstructures termed defended oscillating membrane equipped structures (DOMES) are integrated in the microchannels. These dome-shaped pore-containing DOMES are created above a through hole in the films using two-photon polymerization. As the bottom side of the air-liquid interfaces trapped in DOMES' pores is always facing ambient air, bubble instability that compromises acoustofluidic performance in conventional cases is alleviated or avoided. The acoustically induced flow is observed to be stronger with increasing pore size on DOMES. An acoustofluidic micromixer is proposed to further investigate the capabilities of DOMES, and it is the first time active micromixer is achieved on lab-on-a-foil devices, with good performance competitive to reported microfluidic mixers.

### 1. Introduction

Microfluidics-based lab-on-a-chip devices have become an important tool in a variety of research fields nowadays [1], as evidenced by ever-increasing number of studies and applications [2,3]. Despite diverse materials being applied, most microfluidic devices developed hitherto are fabricated using polydimethylsiloxane (PDMS) due to its excellent properties, such as optical transparency [4], chemical inertness [5], and biocompatibility [6]. However, the fabrication is still challenging for reentrant structures and complex three dimensional (3D) geometries using soft lithography, the most popular method used to create PDMS-based devices [7,8]. Therefore, these devices may not be the best choices in certain situations, especially when it comes to prototype designs.

Recently, lab-on-a-foil has emerged as a promising research concept with applications in nucleic acid analysis [9,10], biosensors [11], robotics [12], electrochemistry [13], and so forth [14]. In contrast to PDMS counterparts, lab-on-a-foil devices use thin and flexible films as substrates. These devices often show great cost effectiveness, ease of fabrication, and simplicity of use [15]. As lab-on-a-foil devices consume little materials, they are often disposable and are considered as environmentally friendly [16]. Moreover, these devices were expected to find huge potential in wearable devices [17], thus contributing to future development of Internet of Things and healthcare services.

At present, various fabrication methods have been proposed to create lab-on-a-foil devices, including micro-thermoforming [18], hot embossing [19], laser micromachining [20], dry resist fabrication [14],

and xurography [21]. Among them, xurography is often considered as the simplest and cheapest. It relies on a knife plotter to cut thin films, in which microchannels are created. The cut films are then covered with bottom and top layers for enclosed flow paths, and reliable bonding between layers can be achieved using off-the-shelf materials such as adhesive tapes [22].

Nonetheless, due to size limitation of the knives, the resolution of xurography is relatively low compared to that of soft lithography [22]. Additionally, it is not easy to integrate more functions on these devices other than fluid transportation inside the microchannels created. Therefore, further adoption of the xurography technology for microfluidics is compromised. In this paper, we propose a novel method to overcome this downside by imparting high-resolution 3D microstructures into xurography-made devices using two-photon polymerization (TPP). This fabrication technique is one of the additive manufacturing technologies working at microscale [23,24], and possessing extremely high resolution (~100 nm) [25].

Owing to its non-invasive manner and the capabilities in manipulating fluids and particles [26,27], acoustofluidics has become an important branch in microfluidics. For instance, as the flow of fluids in microchannels is usually laminar [28], it is challenging to achieve homogenous mixing naturally due to dominance of viscous forces. To address this problem, acoustofluidics can be used to create efficient micromixers. Generally speaking, acoustic energy induces the pressure fluctuations inside microchannels, giving rise to disturbances for the laminar flows. In addition, bubbles, sharp edges, and solid membranes have also been coupled with acoustic fields to improve the performance

\* Corresponding author.

E-mail address: [jiexu@uic.edu](mailto:jiexu@uic.edu) (J. Xu).

<https://doi.org/10.1016/j.snb.2019.02.050>

Received 1 November 2018; Received in revised form 7 February 2019; Accepted 11 February 2019

Available online 12 February 2019

0925-4005/© 2019 Elsevier B.V. All rights reserved.

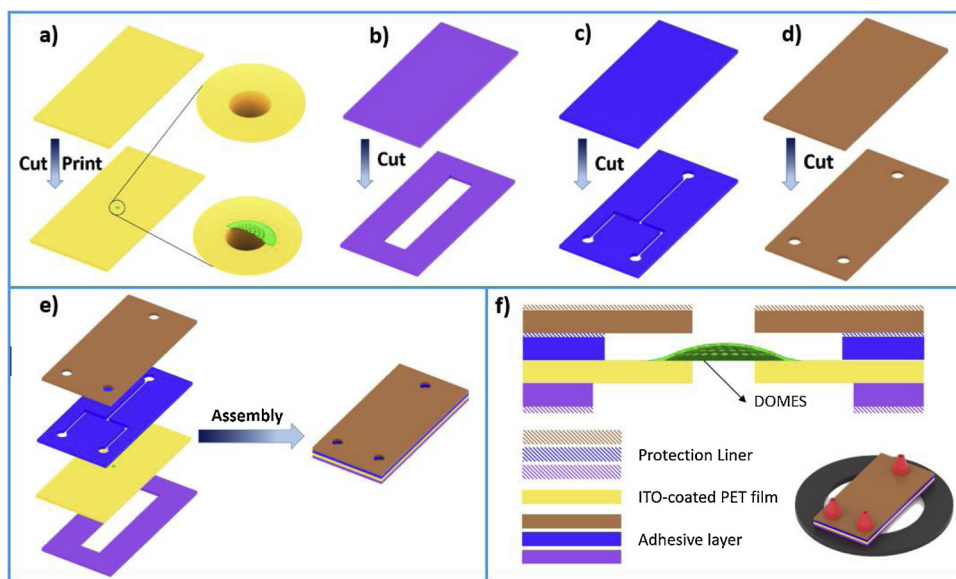


**Fig. 1.** Schematic illustration of the fabrication process for a lab-on-a-foil device integrated with DOMES. a) A circular through hole was first cut in a PET film, and then DOMES was printed above the hole using TPP; b) Double sided tape with a large rectangular hole in the center was prepared using xurography; c) Microchannels were also cut in the tape using xurography; d) Similarly, inlets and outlets were prepared for the top layer; e) Afterwards, all the layers were aligned and bonded with a homemade tool; f) The as-prepared lab-on-a-foil device can be attached to other objects such as piezoelectric instruments and external tubings after revealing the adhesive layers on both sides.

[29–33]. As an example, lateral cavity acoustic transducers (LCATs) based on acoustic bubbles were employed in multiple applications, including micropumps [34], particle sorting [35], and microfluidic switches [36]. Similarly, sharp edges were also applied for the developments of micromixers [32], chemical signal generators [37], and micropumps [38].

However, it is difficult to integrate these components in xurography-based microfluidic devices. A serpentine cut in the films for sidewall cavities or sharp edges usually results in ragged edges and undesired debris. On the other hand, TPP is a superior method to create microscopic high-resolution components, yet direct construction of entire macroscopic devices using TPP would be impractical due to its low fabrication speed [7]. Given the fact that TPP fabrication time is positively proportional to the volume of printed structures, it is possible to print only the key components in a device. Here, we propose using TPP to fabricate structures inside a xurography-made device making it an acoustofluidic lab-on-a-foil.

In conventional acoustofluidic applications, acoustic bubbles often suffer from instability and dissolution [39,40]. For instance, the trapped bubbles tend to expand into microchannels at high flow rates [40], and grow or shrink upon diffusion based on saturation status of the fluids [41]. To solve this problem, Bertin and coworkers proposed a new type of microbubbles (i.e., armored microbubble) [39]. Specifically, a hollow-capsule-shaped microstructure was created to trap bubbles and prevent the dissolution. Longer lifetime of bubbles was achieved compared to those unprotected ones. However, because these microbubbles were still standalone, their lifetime remained short (1 min) when exposed to acoustic actuation.

To prolong the lifetime of acoustic bubbles, or air-liquid interfaces/membranes *per se*, we propose to connect the oscillating membranes with ambient air instead of using bubbles with finite volumes. Briefly speaking, thin shell microstructures with multiple circular pores for trapping membranes are fabricated via TPP and then integrated into devices prepared by xurography. We term these dome-shaped pore-bearing microstructures as defended oscillating membrane equipped structures (DOMES). As they are created above through holes in the films, the bottom side of membranes is always facing ambient air, and gas diffusion into the liquid is compensated by the atmosphere. Hence, the membrane instability is expected to be alleviated or avoided. Moreover, since the pores on DOMES are generally small, watertight condition for the fluids in the microchannels is achievable if the pressure difference between two sides remains small. In this paper, we will first investigate the performance of DOMES, and then create a

micromixer on the foil as an acoustofluidic lab-on-a-foil demonstration. To the best of our knowledge, it is the first time such an active micromixer is achieved in lab-on-a-foil devices.

## 2. Material and methods

### 2.1. Overall fabrication process

We used indium tin oxide (ITO)-coated polyethylene terephthalate (PET) films (127  $\mu\text{m}$  in thickness, Sigma-Aldrich, St. Louis) as the substrates to create lab-on-a-foil devices. PET is a common thermoplastic polymer, and possesses several advantages [15,19,42], including optical transparency, physical, chemical and mechanical stability, as well as good flexibility. ARcare<sup>®</sup> 90445 double-sided adhesive tape (kindly provided by Adhesives Research, Glen Rock, PA) was used for bonding different layers. It is a transparent medical grade tape with good biocompatibility and aqueous insolubility [43–45]. Desktop cutting plotter (QuicKutz Silhouette SD, QuicKutz, Inc., Lindon, UT) was applied for xurography. General fabrication process of a lab-on-a-foil device integrated with DOMES is divided into the following steps:

A 200  $\mu\text{m}$  diameter through hole was first cut in the film using a milling machine (CNC Mini-Mill/3, Minitech Machinery Corp., Atlanta, GA). TPP system (Nanoscribe Photonic Professional GT, Nanoscribe GmbH, Germany) was then used to fabricate DOMES above the hole (Fig. 1a). Since we attach the final device to a piezoelectric actuator, a layer of double-sided tape was added to the bottom of the device. A big rectangular opening was cut in the center to maintain DOMES connection with ambient air (Fig. 1b). Microfluidic channels with 600  $\mu\text{m}$  width were similarly created in the tape layer above the film as shown in Figs. 1c and S1. Inlets and outlets were cut for the top layer (Fig. 1d). Afterwards, all the layers were carefully aligned and pushed together (Fig. 1e) with the help of a homemade alignment tool composed of a three-axis linear stage and a USB digital microscope. Finally, the as-prepared device was clamped between two pieces of glass slide and baked overnight to remove the bubbles trapped during assembly (Fig. S2). To connect the device to external components, adhesive layers can be revealed after peeling off the protection liners on both sides (Fig. 1f). In our cases, the device was bonded to a ring-shaped piezo (APC International, Mackeyville, PA), and tubings were attached through flangeless ferrules (P-200NX, Upchurch Scientific, Oak Harbor, WA) (Fig. S3).

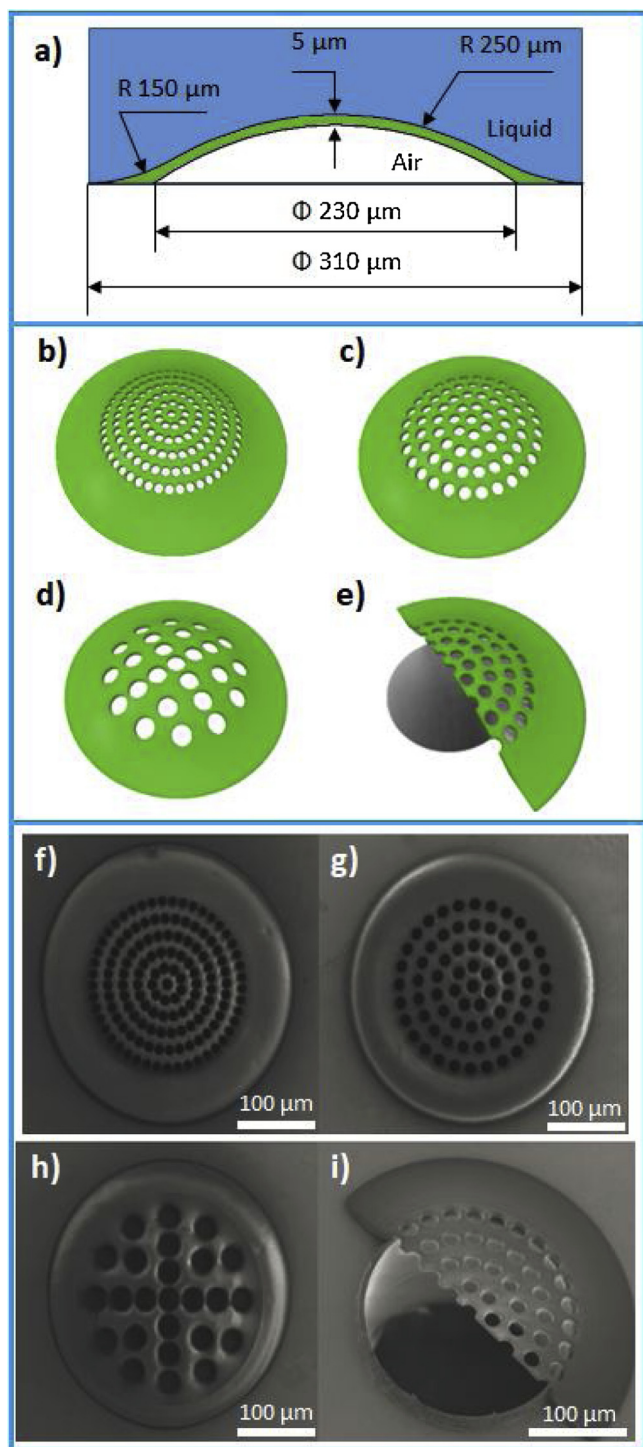


**Fig. 2.** Schemes of different types of DOMES and their corresponding SEM images. a) Side view of a general DOMES structure with dimensions; b–d) Schemes of DOMES with 10.5, 14.55, and 25  $\mu\text{m}$  diameter pores, respectively; e) Scheme of a half DOMES created above a through hole; f–h) Corresponding SEM images of the DOMES with 10.5, 14.55, and 25  $\mu\text{m}$  diameter pores, respectively. i) SEM image of the half DOMES. The tilt angle is 30-degree.

## 2.2. DOMES fabrication

In this study, three types of DOMES were constructed, and all of them had the same contour except for the size and quantity of the pores. As shown in Fig. 2a, DOMES is a dome-shaped pore containing shell with an external diameter of 310  $\mu\text{m}$ , an internal diameter of 230  $\mu\text{m}$ , a

curvature radius of 250  $\mu\text{m}$ , and a thickness of 5  $\mu\text{m}$ . To further study the acoustically induced flow (i.e., microstreaming) with respect to the pore size, the total area of pores for all three types was kept identical. Specifically, the first type of DOMES had 136 pores with a diameter of 10.5  $\mu\text{m}$  (Fig. 2b). The second type had 71 pores with a diameter of 14.55  $\mu\text{m}$  (Fig. 2c), and the third one had 25 pores with a diameter of 25  $\mu\text{m}$  (Fig. 2d). Additionally, a half DOMES was also constructed (Fig. 2e), illustrating how the DOMES was created above the hole with bottom side facing ambient air.

For printing microstructures on PET films, we used the same method applied in our previous article [46]. Basically, the PET film was thoroughly cleaned using acetone, isopropyl alcohol, and then blow-dried with nitrogen. Afterwards, the PET film was mounted on a TPP holder with tape. To avoid the bending of films during fabrication, a glass slide (length of 25 mm and thickness of 0.7 mm, Nanoscribe GmbH, Germany) was placed beneath as a support. A small drop of photoresist (IP-S, Nanoscribe GmbH, Germany) was then dropped onto the top of the through hole at ITO-coated side. The ITO (around 130 nm thick) coating enabled a quick searching for the interface between PET film and IP-S during printing, due to their difference in refractive indices. After applying adaptive slicing of 1  $\mu\text{m}$  with a minimal distance of 0.2  $\mu\text{m}$ , and a hatching of 0.3  $\mu\text{m}$ , the total fabrication time was found to be 3 min. Additionally, we adjusted the coordinates of the TPP system to match that of the DOMES designs using NanoWrite software (Nanoscribe GmbH, Germany) [7]. After printing, excessive photoresist was developed using propylene glycol monomethyl ether acetate (MicroChem, Newton, MA), and the device was dried in the air. The scanning electron microscope (SEM) images of all three designs were shown in Fig. 2f, g, h, respectively. Despite the fact that the gap between each pore in DOMES was only 2  $\mu\text{m}$ , the hatching and slicing distances applied did not lead to any deformation or undesired discrepancies. Additionally, the SEM image of the half DOMES further indicated a good alignment between the printed microstructure and the hole (Fig. 2i).

## 2.3. Driving frequency determination

To determine the driving frequency at which DOMES exert the strongest acoustic microstreaming effect, a free surface PET device without further assembly was attached to a ring-shaped piezo using double-sided tape, and the DOMES on the film had 14.55  $\mu\text{m}$  diameter pores. One drop (around 10  $\mu\text{L}$ ) of deionized (DI) water with green aqueous fluorescent particles (2.0  $\mu\text{m}$  Fluoro-Max dyed polystyrene microspheres, Thermo Fisher Scientific, Waltham, MA) was then added onto the film. Then, a waveform generator (DG1022U; Rigol Technologies Inc., Beijing, China) was used to generate square wave, followed by the amplification via a voltage amplifier (Tegam 2350, Tegam Inc., Madison, OH).

The driving frequency was swept from 100 Hz to 100 kHz at 5 Vpp, and the performance of acoustic microstreaming was determined based on average velocity of the particles. The particles were excited using a fluorescence illuminator (X-cite 120, Lumen Dynamics, Ontario, Canada), and their trajectories were tracked using a high speed camera (Phantom Miro M310, Vision Research Inc., USA) associated with an inverted microscope system (Nikon Eclipse Ti-S, Nikon Instruments Inc.). Phantom Camera Control software (Vision Research, Wayne, NJ) was applied to analyse the results. At frequency of 32.60 kHz, the DOMES was found to exert strongest microstreaming, thus it was used as the driving frequency for the rest of this study.

## 3. Results and discussion

As aforementioned, DOMES is fabricated above a through hole, and its bottom side is always facing ambient air. Therefore, the instability of the membranes trapped is expected to be alleviated or avoided. In this section, after a brief discussion of theoretical background of oscillating

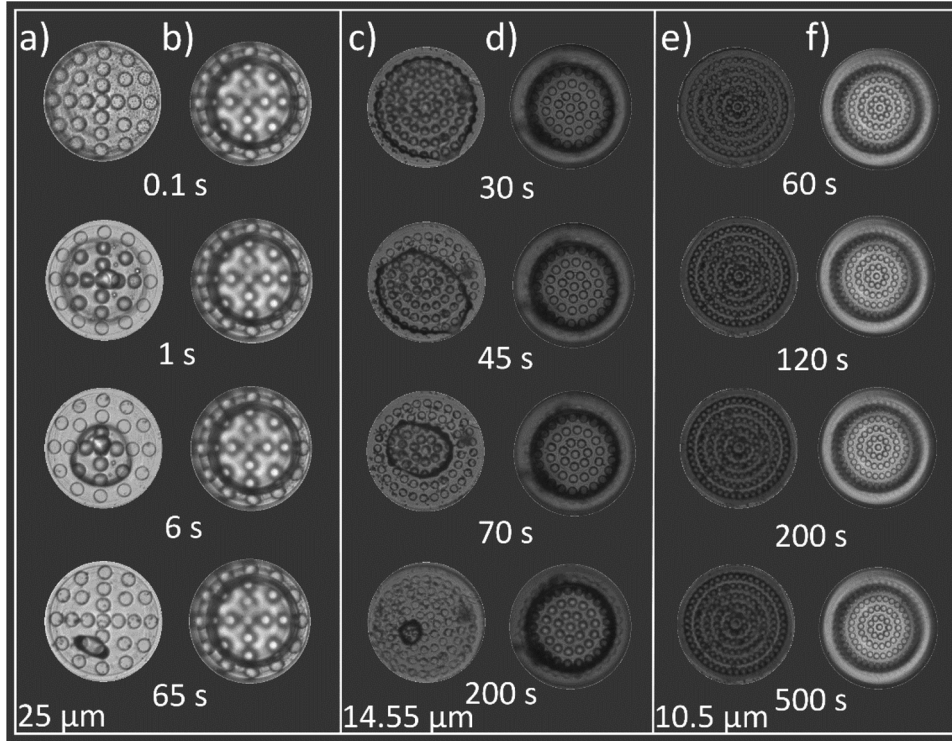


**Fig. 3.** Stability study of the air-water membranes on DOMES without and with through holes upon the actuation of acoustic microstreaming. a–b) DOMES with 25  $\mu\text{m}$  pores created without and with through holes, respectively. c–d) DOMES with 14.55  $\mu\text{m}$  pores created without and with through holes, respectively. e–f) DOMES with 10.5  $\mu\text{m}$  pores created without and with through holes, respectively.

membranes, we report experimental study on the impact of through holes on membrane stability. As expected, the through holes underneath DOMES was observed to enable longer lifetimes of the membranes. We also studied the influence of DOMES pore size on acoustic performance. It was found that the larger the pore size was, the stronger acoustic effects the DOMES could induce, although larger pores were more susceptible to leaking. Finally, we built a micromixer on a lab-on-a-foil device to further validate the capabilities of DOMES for acoustofluidic applications, and competitive performance was achieved compared to those devices made by PDMS.

### 3.1. Theoretical background

In our previous study [27], we derived an explicit expression for the displacement of a thin clamped circular membrane,

$$W(r, \theta, t) = w(r, \theta)e^{i\omega t} \quad (1)$$

where  $w(r, \theta)$  is the solution of:

$$\nabla^4 w(r, \theta) - \kappa^4 w(r, \theta) = 0 \quad (2)$$

with the boundary conditions:

$$w(a, \theta) = 0, \quad \frac{\partial w}{\partial r}(a, \theta) = 0 \quad (3)$$

That is, the oscillation amplitude of the membrane reads:

$$w(r, \theta) = \left( J_n(\kappa a) - \frac{J_n(\kappa a)}{I_n(\kappa a)} I_n(\kappa r) \right) (A_1 \cos(n\theta) + B_1 \sin(n\theta)) \quad (4)$$

Here  $W$  is the time-dependent membrane displacement, and  $w$  is the classical solution for the displacement equation of a thin clamped circular membrane (Eq. (2));  $a$ ,  $\kappa$  stand for the radius of the membrane and wave number, respectively;  $J_n$ ,  $I_n$  stand for the type one and modified Bessel functions, respectively;  $A_1$ ,  $B_1$  are the arbitrary constants. As the pore size in DOMES increases, the membrane displacement increases, and we expect the microstreaming effect to become stronger with more energy dissipated.

Watertightness is another key factor subjected to the pore size, and

the maximum size can be ideally determined using Eq. (5),

$$d = \frac{4\sigma \cos\varphi}{\Delta P} \quad (5)$$

where  $d$  is the maximum pore size that is free from liquid leakage;  $\sigma$ ,  $\varphi$  denote the surface tension, and the contact angle of the liquid, respectively;  $\Delta P$  is the pressure difference between two sides of the membrane. Although this formula does not take into account the interaction between the oscillating membrane with liquid, it provides a straightforward reference when designing the DOMES. For instance, water is one of the most commonly used liquids in microfluidic applications, its surface tension at 298 K is 0.072 kg/s<sup>2</sup>, and the contact angle between water and the material of DOMES (i.e., IP-S) is 73.8° [25]. As a result, the pressure barriers (maximum pressure at which the pore still maintains watertightness) for the pores with diameter of 10.5, 14.55, and 25  $\mu\text{m}$  are 3840, 2772, and 1613 Pa, respectively.

To verify these results, DOMES with different pore sizes were integrated in straight microchannels, in which only the inlet was left for water injection while the outlet was sealed. Hence, the pores on DOMES became the only possible exits for liquids. The pressure difference exerted was varied upon changing the gravitational potential of the water reservoir (Fig. S4). We found that the actual pressure barriers were 3530, 2620, and 1530 Pa for DOMES with 10.5, 14.55, and 25  $\mu\text{m}$  diameter pores, respectively. The results indicated a good agreement with the theoretical prediction.

### 3.2. Impact of the through hole and pore size

In order to understand the role of through holes in compensating the vulnerability of conventional bubbles due to gas dissolution and acoustic pressure fluctuations, a series of free surface devices with or without through holes was actuated at 5 Vpp.

The results in Fig. 3 indicated that standalone bubbles trapped in the DOMES built on films without holes were more vulnerable compared to those with holes. The bubble trapped in DOMES with 25  $\mu\text{m}$  pores gradually disappeared as time passed (Fig. 3a). This can be attributed to its small pressure barrier. Specifically, after water

penetrated the pores, the bubble was first compressed, and then dissolved until completely gone. As a result, corresponding microstreaming gradually became weaker and finally disappeared. On the other hand, the membranes in DOMES on through hole were remained intact after the piezoelectric transducer was turned on (Fig. 3b), and the microstreaming remained the same for more than 30 min. This suggested that the problem of gas dissolution was alleviated.

As the pore size decreases, the pressure barrier and flow resistance increases, making water penetration more difficult, giving rise to a slower shrinkage of the bubbles. For instance, the bubble trapped in DOMES with 14.55  $\mu\text{m}$  pores became negligible after 200 s with acoustic energy being turned on (Fig. 3c), while it took only 65 s for 25  $\mu\text{m}$  pores. Note that, the membranes in the DOMES with 10.5  $\mu\text{m}$  pores remained almost the same after 500 s, indicating a stronger bubble stability due to large pressure barrier (Fig. 3e). Similarly, the membranes on DOMES above the through holes also underwent no change (Fig. 3d, f).

We further studied the acoustic performance of DOMES with respect to the pore size (Video 1). The first device was created using an intact film (no through holes), while the second to fourth devices were created using films with through holes. To obtain a straightforward and clear comparison, 24 frames that formed a complete 1-second video clip were superimposed (Fig. 4). This way, particles become less visible in faster flow field. The result shows that first device (i.e., DMOES without through hole underneath) produced weak microstreaming, since the trajectories of particles can be clearly seen (Fig. 4a). For devices with DOMES on through holes, only blurry particle trajectories were observable indicating stronger microstreaming field. Additionally, DOMES with larger pore size exhibited stronger performance. For instance, trajectories were observable in the microstreaming induced by small pores (Fig. 4b, c), but can be barely noticed for large pores (Fig. 4d). Such a trend matches our predication mentioned in Section 3.1.

Nonetheless, liquid leakage can be an issue for large pores. After turning the free surface devices into enclosed ones, DOMES with 25  $\mu\text{m}$  diameter pores were no longer able to maintain watertightness, further giving rise to weaker microstreaming. This can be attributed to the pressure drop inside microchannels and the acoustic pressure (around 1100 Pa, measured with a H2a-XLR hydrophone (Aquarian Audio)). Moreover, returning flows from the channel walls may also pose

additional hydrodynamic pressure [47].

### 3.3. Lab-on-a-foil acoustofluidic application

To further prove the feasibility of using DOMES for lab-on-a-foil applications, an acoustofluidic micromixer was built and tested as a demonstration. Given that 25  $\mu\text{m}$  pores could not hold membranes well, 14.55  $\mu\text{m}$  pores was adopted. The device included a T-shaped microchannel with two inlets and one outlet (Fig. 5). The length and the width of the microchannels were 6 mm and 600  $\mu\text{m}$ , respectively. DOMES (green spot in Fig. 5) was carefully aligned in the centre of the main channel. After assembly, the device was bonded onto a ring-shaped piezo, and connected with tubings (Fig. S3c). Additionally, DI water and DI water with fluorescent dye (Fluorescein sodium salt, Sigma-Aldrich, St. Louis) were used as two mixing fluids. To quantitatively characterize the performance of mixing, relative mixing index (RMI) was calculated at a measuring line 600  $\mu\text{m}$  away from the centre of DOMES after mixing (see the dashed line in Fig. 5). In contrast to conventional mixing indices involving rescaling and stretching of grayscale intensities, RMI was used here to preclude the influence of lighting conditions [28]. It is calculated as follows:

$$RMI = 1 - \frac{\sqrt{\frac{1}{N} \sum_{i=1}^N (I_i - \langle I \rangle)^2}}{\sqrt{\frac{1}{N} \sum_{i=1}^N (I_{oi} - \langle I \rangle)^2}} \quad (6)$$

where  $N$  denotes the number of pixels in the measuring region;  $I_i$  and  $I_{oi}$  denote the local intensity of the  $i$ -th pixel after and before mixing, respectively;  $\langle I \rangle$  indicates the average of pixel intensities in the region. Here, a RMI of 0 denotes an unmixed status, while 1 indicates thoroughly mixing. In addition, a threshold of 0.75 was selected as a criterion to determine acceptable mixing performance.

Mixing performance was first investigated by applying a series of voltages ranging from 1 to 8 V (Video 2) at flow rate of 4  $\mu\text{l}/\text{min}$  for each fluid. As illustrated in Figs. 5 and 6, the mixing performance was improved and plateaued with increasing driving voltage. Since the intensity of microstreaming grows quadratically with driving voltage [48], the mixing index increased rapidly from 1 to 4 V, and acceptable mixing was achieved after 4 V. Another way of quantifying mixing performance is to look at mixing time  $\tau$ :

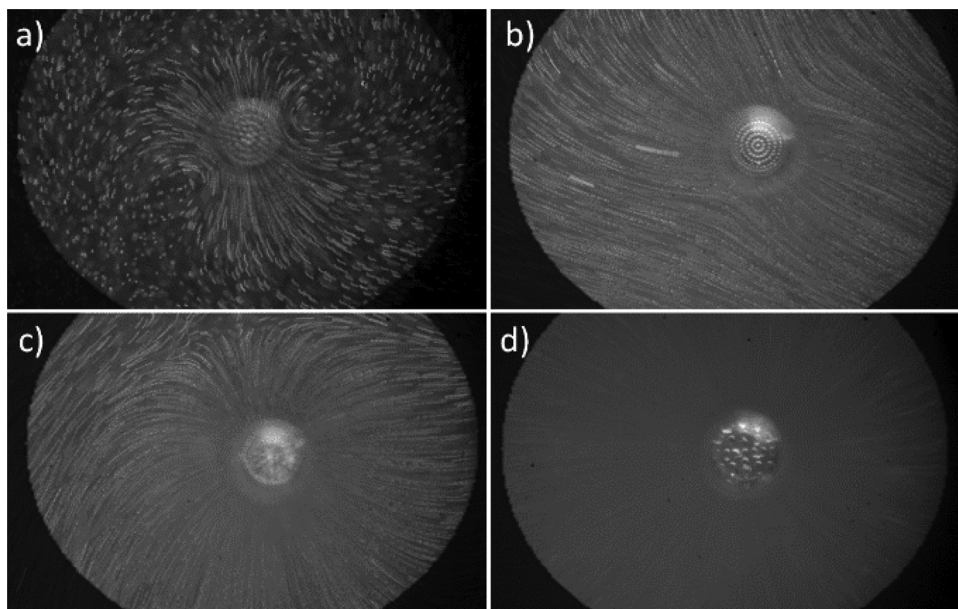


Fig. 4. Acoustic microstreaming induced by different DOMES: a) DOMES fabricated on an intact film. b–d) DOMES with different pore sizes (10.5, 14.55, and 25  $\mu\text{m}$ , respectively) fabricated above a through hole.

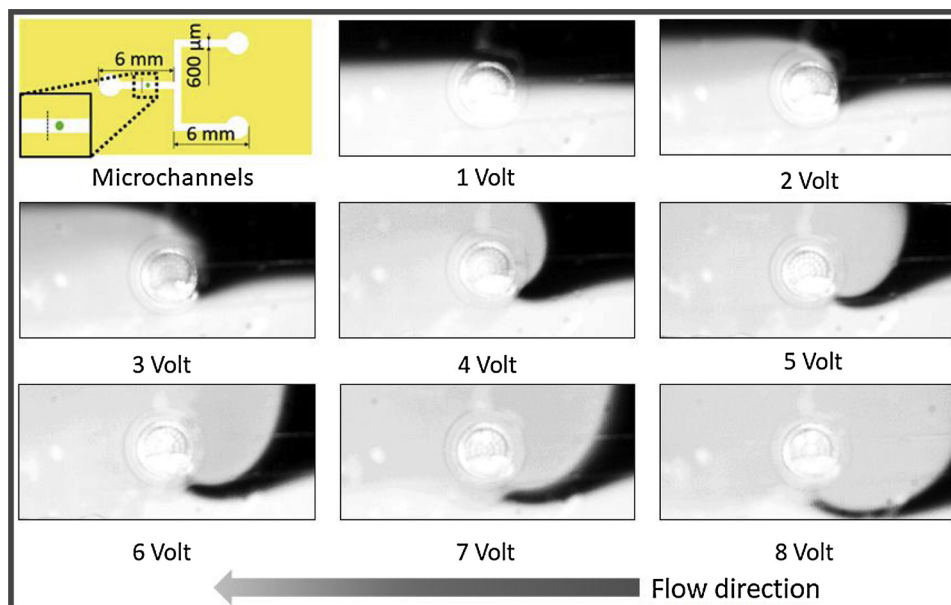


Fig. 5. Scheme of the microchannels with dimensions, as well as images showing the mixing performance at different driving voltages ranging from 1 to 8 V.

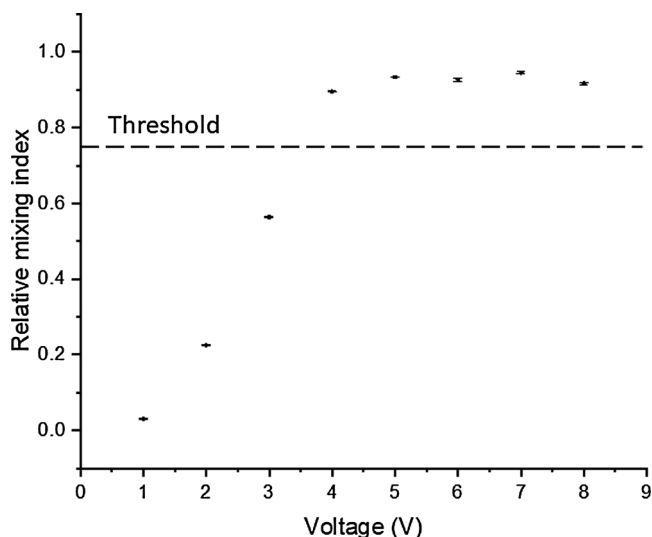


Fig. 6. Plot of the mixing index versus driving voltage.

$$\tau = L/v \quad (7)$$

where  $L$  is the mixing length, and  $v$  is the average fluid velocity. Mixing length is usually defined as the distance between the mixer and the downstream location where complete mixing is achieved. In our experiments, we noticed that as the driving voltage became larger, the microstreaming pattern also became larger and even extended into upstream areas. This phenomenon made mixing even happen before fluid reaching the location of DOMES at voltages greater than 4 V. Therefore, we can consider the mixing length  $L$  to be 0, proving the potential of DOMES for immediate mixing.

In addition, we investigated the impact of flow rate on mixing performance at 5 V. Flow rate ranging from 4 to 20  $\mu\text{l}/\text{min}$  were applied to each fluid (Video 3), and acceptable mixing was obtained when the flow rate was equivalent or smaller than 8  $\mu\text{l}/\text{min}$  (Figs. 7 and 8). When the flow rate increased to 8  $\mu\text{l}/\text{min}$ , the mixing index reached the threshold value set previously (0.75). In this case, the mixing length can be considered as the distance from measuring line to the centre of DOMES (i.e., 600  $\mu\text{m}$ ), from which a mixing time was calculated to be 87.8 ms. As aforementioned, it was the first time such an active

micromixer was achieved in lab-on-a-foil devices, and the mixing time was competitive even compared to most PDMS microfluidic mixers.

#### 4. Conclusions

In summary, a novel type of microstructures termed DOMES was proposed for lab-on-a-foil acoustofluidic applications. The devices were created using off-the-shelf PET films and double-sided tapes via xurography. DOMES was fabricated by two-photon polymerization and integrated in the microchannels. Compared with regular standalone acoustic bubbles, the bottom side of the air-liquid interfaces on DOMES was always facing ambient air, thanks to the through hole underneath the DOMES. Moreover, common dissolution and compression problems of acoustic bubbles were alleviated, giving rise to a more stable performance. We also investigated the role of pores on DOMES. It was observed that as the pore size increased, the microstreaming induced by DOMES became stronger. However, the pressure tolerance decreased in the meanwhile, which may lead to liquid leakage rather than maintaining watertightness. To further prove the capabilities of DOMES in acoustofluidic applications, a micromixer was demonstrated. We found that the mixing efficiency was improved upon the increase of driving voltage, and acceptable mixing was obtained when the voltage was equal to or greater than 4 V at 4  $\mu\text{l}/\text{min}$  (each fluid). Additionally, acceptable mixing can be realized when the flow rate was reduced to 8  $\mu\text{l}/\text{min}$  at 5 V, and the mixing time was 87.8 ms at 8  $\mu\text{l}/\text{min}$ . The results suggested that the first acoustofluidic micromixer on the foil possessed a comparable performance compared to those devices fabricated using PDMS.

Admittedly, although xurography itself is cheap and simple, the acoustofluidic performance mainly came from DOMES, which was fabricated using TPP, a technology nowadays is still expensive and not widespread. Nonetheless, methods such as molding or low-cost micro-scale 3D fabrication techniques may be applied to address this downside in the future. For instance, 3D microfabrication was achieved using a thin multimode optical fibre recently [49], and it did not require bulky and expensive femtosecond laser while maintaining excellent resolution. Alignment and bubble removal process also bring the inconvenience to the fabrication process, yet these problems can be addressed using automation machines when it comes to mass production. Despite the aforementioned limitations, we believe that the proposed acoustofluidic lab-on-a-foil devices open a door for a variety of

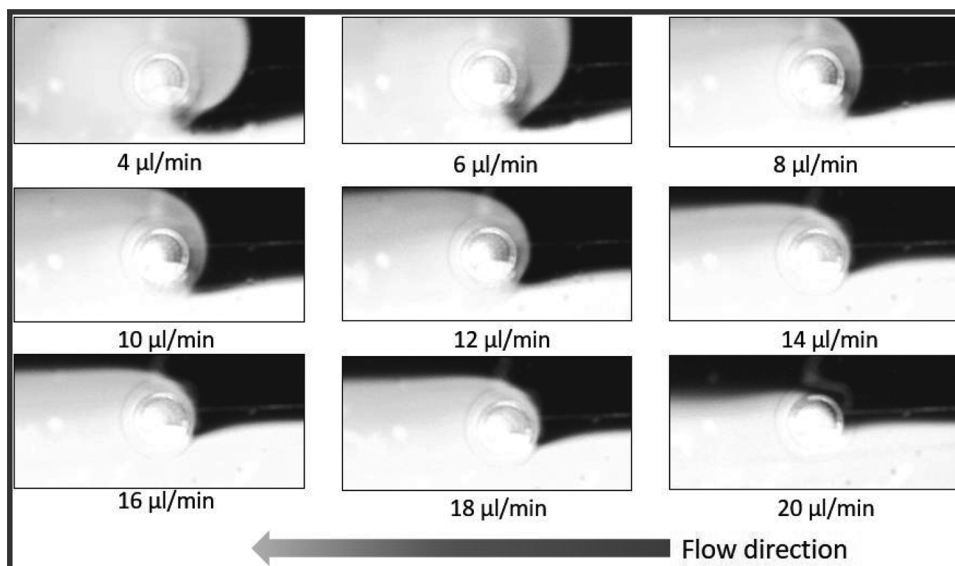


Fig. 7. Images indicating the mixing performance at different flow rates ranging from 4 to 20  $\mu\text{l}/\text{min}$ .

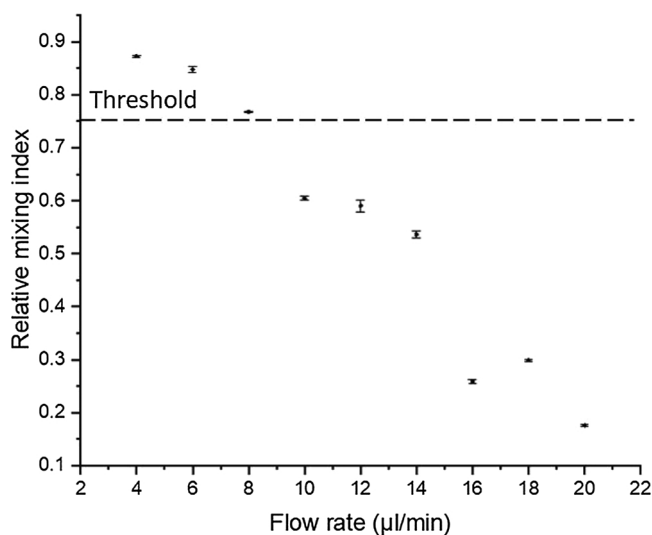


Fig. 8. Plot of the mixing index versus flow rate.

potential microfluidic applications in the future.

#### Conflicts of interest

The authors declare no conflict of interest.

#### Acknowledgements

This work was supported by an Early Career Faculty grant (8ONSSC17K0522) from NASA's Space Technology Research Grants Program, USA.

#### Appendix A. Supplementary data

Supplementary material related to this article can be found, in the online version, at doi:<https://doi.org/10.1016/j.snb.2019.02.050>.

#### References

- [1] G.M. Whitesides, The origins and the future of microfluidics, *Nature* 442 (2006) 368.
- [2] P. Gravesen, J. Branebjerg, O.S. Jensen, Microfluidics—a review, *J. Micromech. Microeng.* 3 (1993) 168.
- [3] P. Kim, K.W. Kwon, M.C. Park, S.H. Lee, S.M. Kim, K.Y. Suh, *Soft Lithography for Microfluidics: A Review*, (2008).
- [4] J.O. Hwang, D.H. Lee, J.Y. Kim, T.H. Han, B.H. Kim, M. Park, et al., Vertical ZnO nanowires/graphene hybrids for transparent and flexible field emission, *J. Mater. Chem.* 21 (2011) 3432–3437.
- [5] C.-Y. Li, Y.-C. Liao, Adhesive stretchable printed conductive thin film patterns on PDMS surface with an atmospheric plasma treatment, *ACS Appl. Mater. Interfaces* 8 (2016) 11868–11874.
- [6] A. Folch, *Introduction to bioMEMS*, CRC Press, 2016.
- [7] Y. Lin, C. Gao, D. Gritsenko, R. Zhou, J. Xu, *Soft lithography based on photolithography and two-photon polymerization*, *Microfluid. Nanofluid.* 22 (2018) 97.
- [8] C.N. LaFratta, T. Baldacchini, R.A. Farrer, J.T. Fourkas, M.C. Teich, B.E. Saleh, et al., Replication of two-photon-polymerized structures with extremely high aspect ratios and large overhangs, *J. Phys. Chem. B* 108 (2004) 11256–11258.
- [9] K. Shen, X. Chen, M. Guo, J. Cheng, A microchip-based PCR device using flexible printed circuit technology, *Sens. Actuators B Chem.* 105 (2005) 251–258.
- [10] P. Lin, X. Luo, I.M. Hsing, F. Yan, Organic electrochemical transistors integrated in flexible microfluidic systems and used for label-free DNA sensing, *Adv. Mater.* 23 (2011) 4035–4040.
- [11] J.-C. Chou, Y.-L. Tsai, T.-Y. Cheng, Y.-H. Liao, G.-C. Ye, S.-Y. Yang, Fabrication of arrayed flexible screen-printed glucose biosensor based on microfluidic framework, *IEEE Sens. J.* 14 (2014) 178–183.
- [12] R.D.P. Wong, J.D. Posner, V.J. Santos, Flexible microfluidic normal force sensor skin for tactile feedback, *Sens. Actuators A Phys.* 179 (2012) 62–69.
- [13] J. Chen, Y. Zhou, D. Wang, F. He, V.M. Rotello, K.R. Carter, et al., UV-nanoimprint lithography as a tool to develop flexible microfluidic devices for electrochemical detection, *Lab Chip* 15 (2015) 3086–3094.
- [14] M. Focke, D. Kosse, C. Müller, H. Reinecke, R. Zengerle, F. von Stetten, Lab-on-a-Foil: microfluidics on thin and flexible films, *Lab Chip* 10 (2010) 1365–1386.
- [15] S. Wang, T. Chinnasamy, M.A. Lifson, F. Inci, U. Demirci, Flexible substrate-based devices for point-of-care diagnostics, *Trends Biotechnol.* 34 (2016) 909–921.
- [16] G.S. Fiorini, D.T. Chiu, Disposable microfluidic devices: fabrication, function, and application, *BioTechniques* 38 (2005) 429–446.
- [17] Y. Liu, M. Pharr, G.A. Salvatore, Lab-on-skin: a review of flexible and stretchable electronics for wearable health monitoring, *ACS Nano* 11 (2017) 9614–9635.
- [18] R. Truckenmüller, S. Giselbrecht, C. van Blitterswijk, N. Dambrowsky, E. Gottwald, T. Mappes, et al., Flexible fluidic microchips based on thermoformed and locally modified thin polymer films, *Lab Chip* 8 (2008) 1570–1579.
- [19] J. Li, C. Liu, H. Qiao, L. Zhu, G. Chen, X. Dai, Hot embossing/bonding of a poly (ethylene terephthalate) (PET) microfluidic chip, *J. Micromech. Microeng.* 18 (2007) 015008.
- [20] C.K. Malek, L. Robert, R. Salut, Femtosecond laser machining and lamination for large-area flexible organic microfluidic chips, *Eur. Phys. J.-Appl. Phys.* 46 (2009).
- [21] D.A. Bartholomeusz, R.W. Boutté, J.D. Andrade, Xurography: rapid prototyping of microstructures using a cutting plotter, *J. Microelectromech. Syst.* 14 (2005) 1364–1374.
- [22] P.K. Yuen, V.N. Goral, Low-cost rapid prototyping of flexible microfluidic devices using a desktop digital craft cutter, *Lab Chip* 10 (2010) 384–387.
- [23] H. Xia, J. Wang, Y. Tian, Q.D. Chen, X.B. Du, Y.L. Zhang, et al., Ferrofluids for fabrication of remotely controllable micro-nanomachines by two-photon polymerization, *Adv. Mater.* 22 (2010) 3204–3207.
- [24] S. Kim, F. Qiu, S. Kim, A. Ghanbari, C. Moon, L. Zhang, et al., Fabrication and characterization of magnetic microrobots for three-dimensional cell culture and targeted transportation, *Adv. Mater.* 25 (2013) 5863–5868.

- [25] Y. Lin, J. Xu, Microstructures fabricated by two-photon polymerization and their remote manipulation techniques: toward 3D printing of micromachines, *Adv. Opt. Mater.* 6 (2018) 1701359.
- [26] D. Ahmed, X. Mao, B.K. Juluri, T.J. Huang, A fast microfluidic mixer based on acoustically driven sidewall-trapped microbubbles, *Microfluid. Nanofluid.* 7 (2009) 727.
- [27] D. Gritsenko, Y. Lin, V. Hovorka, Z. Zhang, A. Ahmadianyazdi, J. Xu, Vibrational modes prediction for water-air bubbles trapped in circular microcavities, *Phys. Fluids* 30 (2018) 082001.
- [28] A. Hashmi, J. Xu, On the quantification of mixing in microfluidics, *J. Lab. Autom.* 19 (2014) 488–491.
- [29] A.R. Tovar, A.P. Lee, Lateral cavity acoustic transducer, *Lab Chip* 9 (2009) 41–43.
- [30] R.H. Liu, J. Yang, M.Z. Pindera, M. Athavale, P. Grodzinski, Bubble-induced acoustic micromixing, *Lab Chip* 2 (2002) 151–157.
- [31] A. De Vellis, D. Gritsenko, Y. Lin, Z. Wu, X. Zhang, Y. Pan, et al., Drastic sensing enhancement using acoustic bubbles for surface-based microfluidic sensors, *Sens. Actuators B Chem.* 243 (2017) 298–302.
- [32] P.-H. Huang, Y. Xie, D. Ahmed, J. Rufo, N. Nama, Y. Chen, et al., An acoustofluidic micromixer based on oscillating sidewall sharp-edges, *Lab Chip* 13 (2013) 3847–3852.
- [33] H. Van Phan, M.B. Coşkun, M. Şeşen, G. Pandraud, A. Neild, T. Alan, Vibrating membrane with discontinuities for rapid and efficient microfluidic mixing, *Lab Chip* 15 (2015) 4206–4216.
- [34] A.R. Tovar, M.V. Patel, A.P. Lee, Lateral air cavities for microfluidic pumping with the use of acoustic energy, *Microfluid. Nanofluid.* 10 (2011) 1269–1278.
- [35] M.V. Patel, A.R. Tovar, K.S. Tong, A.P. Lee, Lateral cavity acoustic transducer for particle sorting applications, *The Proceedings of MicroTAS 2009*, (2009).
- [36] M.V. Patel, A.R. Tovar, A.P. Lee, Lateral cavity acoustic transducer as an on-chip cell/particle microfluidic switch, *Lab Chip* 12 (2012) 139–145.
- [37] P.-H. Huang, C.Y. Chan, P. Li, Y. Wang, N. Nama, H. Bachman, et al., A sharp-edge-based acoustofluidic chemical signal generator, *Lab Chip* 18 (2018) 1411–1421.
- [38] P.-H. Huang, N. Nama, Z. Mao, P. Li, J. Rufo, Y. Chen, et al., A reliable and programmable acoustofluidic pump powered by oscillating sharp-edge structures, *Lab Chip* 14 (2014) 4319–4323.
- [39] N. Bertin, T.A. Spelman, O. Stephan, L. Gredy, M. Bouriau, E. Lauga, et al., Propulsion of bubble-based acoustic microswimmers, *Phys. Rev. Appl.* 4 (2015) 064012.
- [40] P.-H. Huang, M. Ian Lapsley, D. Ahmed, Y. Chen, L. Wang, T. Jun Huang, A single-layer, planar, optofluidic switch powered by acoustically driven, oscillating microbubbles, *Appl. Phys. Lett.* 101 (2012) 141101.
- [41] P.S. Epstein, M.S. Plesset, On the stability of gas bubbles in liquid-gas solutions, *J. Chem. Phys.* 18 (1950) 1505–1509.
- [42] Z. Hu, X. Chen, Fabrication of polyethylene terephthalate microfluidic chip using CO2 laser system, *Int. Polym. Process. J. Polym. Process. Soc.* 33 (2018) 106–109.
- [43] D. Patko, Z. Mártonfalvi, B. Kovacs, F. Vonderviszt, M. Kellermayer, R. Horvath, Microfluidic channels laser-cut in thin double-sided tapes: cost-effective bio-compatible fluidics in minutes from design to final integration with optical bio-chips, *Sens. Actuators B Chem.* 196 (2014) 352–356.
- [44] U. Eletxigerra, J. Martinez-Perdiguero, S. Merino, Disposable microfluidic immuno-biochip for rapid electrochemical detection of tumor necrosis factor alpha biomarker, *Sens. Actuators B Chem.* 221 (2015) 1406–1411.
- [45] S. Santiago-Felipe, L.A. Tortajada-Genaro, J. Carrascosa, R. Puchades, Á. Maquieira, Real-time loop-mediated isothermal DNA amplification in compact disc micro-actors, *Biosens. Bioelectron.* 79 (2016) 300–306.
- [46] Y. Lin, R. Zhou, J. Xu, Superhydrophobic surfaces based on fractal and hierarchical microstructures using two-photon polymerization: toward flexible superhydrophobic films, *Adv. Mater. Interfaces* (2018) 1801126.
- [47] H.J. Hussein, S.P. Capp, W.K. George, Velocity measurements in a high-Reynolds-number, momentum-conserving, axisymmetric, turbulent jet, *J. Fluid Mech.* 258 (1994) 31–75.
- [48] J. Xu, D. Attinger, Control and ultrasonic actuation of a gas-liquid interface in a microfluidic chip, *J. Micromech. Microeng.* 17 (2007) 609.
- [49] P. Delrot, D. Loterie, D. Psaltis, C. Moser, Single-photon three-dimensional micro-fabrication through a multimode optical fiber, *Opt. Express* 26 (2018) 1766–1778.